 doi:10.20944/preprints202207.0211.v1

*Article*

# Particle Swarm Optimization and Two-Way Fixed-Effects Analysis of Variance for Efficient Brain Tumor Segmentation

**Naoual Atia[1], Amir Benzaoui[2], Sébastien Jacques[3], Madina Hamiane[4], Kaouther El Kourd[5], Ayache Bouakaz[6], and Abdeldjalil Ouahabi[6,*]**

1 Department of Electrical Engineering, University Mohamed Khider of Biskra, Algeria; naoulatia@yahoo.fr (N.A.);
2 Electrical Engineering Department, University of Skikda, BP 26, El Hadaiek, Skikda 21000, Algeria; a.benzaoui@univ-skikda.dz (A.B.);
3 GREMAN UMR 7347, University of Tours, CNRS, INSA Centre Val-de-Loire, Tours 37100, France; sebastien.jacques@univ-tours.fr (S.J.);
4 College of Engineering, Royal University for Women, West Riffa 37400, Bahrain; mhamiane@ruw.edu.bh (M.H.);
5 Department of Physics, Benyoucef Benkhedda University of Algiers, Algeria; kaouther_youcef@yahoo.fr (K.E.K.);
6 UMR 1253, iBrain, INSERM, Université de Tours, Hospital of Tours, 37000 Tours, France; ayache.bouakaz@univ-tours.fr (Ay.B.) and ouahabi@univ-tours.fr (A.O.).
* Correspondence: ouahabi@univ-tours.fr; Tel.: +33-2-4736-1323 (A.O.)

**Simple Summary:** Segmentation of brain tumor images from magnetic resonance imaging (MRI) is a challenging topic in medical image analysis. The brain tumor can take many shapes, and MRI images vary considerably in intensity, making lesion detection difficult for radiologists. This paper proposes a three-step approach to solve this problem: (1) Preprocessing based on morphological operations is applied to remove the skull bone from the image; (2) The particle swarm optimization (PSO) algorithm with a two-way fixed-effects analysis of variance (ANOVA) based fitness function is used to find the optimal block containing the brain lesion; and (3) The K-means clustering algorithm is adopted to classify the detected block as tumor or non-tumor. An extensive experimental analysis, including visual and statistical evaluations, was conducted on an MRI database privided by the Imaging Center of Kouba in Algiers (Algeria) and shows that the proposed methodology achieves impressive performance compared to several competing approaches.

**Abstract:** Segmentation of brain tumor images is a major research topic in medical imaging to have a refined detection and understanding of abnormal masses in the brain. This paper proposes a new segmentation method, consisting of three main steps, to detect brain lesions using magnetic resonance imaging (MRI). In the first step, the parts of the image delineating the skull bone are removed to exclude insignificant data. In the second step, which is the main contribution of this study, the particle swarm optimization (PSO) technique is applied to detect the block that contains the brain lesions. The fitness function, used to determine the best block among all candidate blocks, is based on a two-way fixed-effects analysis of variance (ANOVA). In the last step of the algorithm, the K-means segmentation method is used in the lesion block to classify it as tumor or not. A thorough evaluation of the proposed algorithm is performed using the MRI database provided by the Kouba imaging center in Algiers, Algeria. Estimates of the selected fitness function are first compared to those based on the sum-of-absolute-differences (SAD) dissimilarity criterion and demonstrate the efficiency and robustness of the ANOVA. The performance of the optimized brain tumor segmentation algorithm is then compared to the results of several state-of-the-art techniques, including fuzzy C-means, K-means, Otsu thresholding, local thresholding, and watershed segmentation. The results obtained using Dice coefficient, Jaccard distance, correlation coefficient, and root mean square error (RMSE) measurements demonstrate the superiority of the proposed optimized segmentation algorithm over equivalent techniques.

**Keywords:** Brain tumor; Image segmentation; PSO; ANOVA, K-means.

 doi:10.20944/preprints202207.0211.v1

## 1. Introduction

### *1.1. What Is a Brain Tumor?*

A brain tumor is a cluster of uncontrolled cancer cells that grow in or around the brain. Brain tumors are divided into two categories: primary tumors, originating in the brain or spinal cord, and secondary tumors, also called brain metastases, which develop elsewhere in the body and spread to the brain [1]. In the first category (i.e., primary tumors), the probability of a person developing this type of tumor in their lifetime is less than 1% [2]. Although this probability is low, for example, in 2020, this still represented just over 308,000 people diagnosed worldwide [3]. A figure that should also alert us is the increased incidence of brain tumors at all ages over the last 20 years. For example, the incidence has increased by more than 40% in adults. In the second category (i.e., secondary tumors), the cancers that most often spread to the brain are breast, kidney, and lung cancers, as well as leukemia, lymphoma, and melanoma [4].

Since a brain tumor can take many forms, it is difficult for radiologists and physicians to diagnose it indisputably because medical imaging images can vary in intensity. To help practitioners make their diagnosis, several approaches to detecting and segmenting brain tumors from magnetic resonance imaging (MRI) images have been proposed in the literature [5−6].

In addition to MRI, functional ultrasound is a modality that is gaining recognition in medicine. It can allow the imaging of the neuronal activity of the brain of small, awake and mobile animals. Nevertheless, such a modality requires long ultrasound acquisitions at high frequency to have an acceptable sensitivity, hence possible material constraints [7].

In addition, during brain tumor surgery, two types of difficulties may arise: (i) identification of the tumor and its boundaries in relation to the healthy brain; (ii) identification of functional brain regions, i.e., those involved in neurological functions (skills, sensitivity, language, vision, cognition, etc.). The gold standard method currently used to improve the quality of brain tumor resection while minimizing neurological risk is so-called "standby" surgery with direct electrical brain stimulation. Practitioners commonly use ultrasound to localize the tumor in the brain, but to date there are no pre- or intraoperative imaging tools to identify functional brain regions [8]. Hence the need for innovative imaging in this area, such as high-frequency Doppler ultrasound in the surgical management of patients with awake brain tumors. Ultrahigh frequency achieves a spatial resolution of 30 μm, and thus more than five times better than MRI. The Doppler mode [9−12] detects microvascular flows at velocities less than 1 mm/second.

### *1.2. Why Be Interested in Brain Tumor Segmentation?*

Being able to locate and delineate the perimeter of the brain tumor is critical to its treatment. Doctors use radiation therapy, chemotherapy and surgery, when possible, to treat these tumors, although the latter is always impressive.

Among the primary tumors, meningiomas affect, as their name suggests, the meninges (see Figure 1), the envelopes that protect the brain, the dura mater, the arachnoid and the piebald. These tumors are often benign, but they can be very disabling. Gliomas are common [13]. For example, in France, there are between 2,500 and 3,000 of them per year [14]. These tumors develop inside the brain from the glial cells that support and nourish the neurons. Gliomas may have different names depending on the type of glial cells involved (e.g., an astrocytoma if astrocytes are involved). Most of the time, gliomas are malignant. This is the case of glioblastoma. Others are “precancerous” forms that can become malignant (like astrocytoma). Finally, rare forms of gliomas are benign and will remain so.

Preprints (www.preprints.org) | NOT PEER-REVIEWED | Posted: 14 July 2022 doi:10.20944/preprints202207.0211.v1

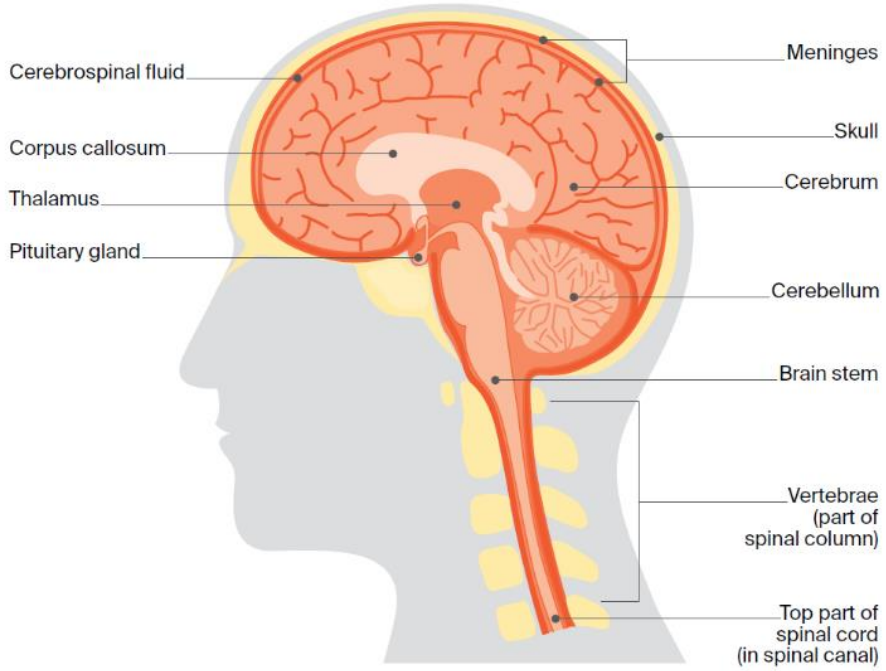


**Figure 1.** Brain cross-section.

The symptoms of brain tumors depend on their location. They may include problems with language, vision, motor skills and balance. Other symptoms are related to the compression of the brain by the tumor, which can cause intracranial hypertension, accompanied by headaches, nausea and vomiting.

Diagnosis is based on imaging (computed tomography also called CT-scan or MRI) and biopsy to determine if the tumor is benign or malignant.

To treat a meningioma, it is possible to perform a surgical procedure for which it is necessary to open the skull bone. The goal of the operation is to remove as much of the cancerous tissue as possible without affecting the healthy brain. A portion of the tumor will be analyzed during the operation to determine its exact nature and to allow the implementation of an adapted treatment after the operation: chemotherapy, radiotherapy...

Sometimes brain tumors are located near sensitive areas such as those that control speech or vision, for example. In order to remove these tumors without affecting these essential functions, surgeons must mark the area. To do this, they must wake the patient during the procedure and put them to work.

The skull must be opened to access the brain and remove a brain tumor. This is called a craniotomy or, in common parlance, a trepanning. This particular procedure is performed under general anesthesia by a neurosurgeon. The procedure involves incising, removing and folding back the scalp, then cutting the bones to create a cranial flap, a bony surface that is folded back or detached during the operation. After surgery, the flap is put back in place and fixed.

In the case of a malignant brain tumor, surgery is often required to remove the lesion. A neuronavigation device can help the surgeon. This software allows the surgeon to precisely guide himself inside the brain. The neuronavigation device, a type of GPS, allows the surgeon to navigate inside the brain. This device allows the surgeon to verify at any time during the operation that he or she is not deviating from the planned trajectory, that he or she is following it well and that he or she will be able to enter directly into the volume of the tumor to remove it completely and verify that it corresponds to the limits defined on the images.

The patient's MRI and CT scans are recorded beforehand. This allows the surgeon to model the brain and the location of the tumor. This data allows the surgeon to guide himself. With his eyes fixed on the operating microscope, the surgeon works his way to the tumor with his ultrasound scalpel. He can then fragment and aspirate the tumor. Using

Preprints (www.preprints.org) | NOT PEER-REVIEWED | Posted: 14 July 2022 doi:10.20944/preprints202207.0211.v1

neuronavigation, the surgeon can also locate and remove other small tumors. Once the tumor is removed, the surgeon closes the skull. Neuronavigation is a valuable aid in this type of surgery [15], but it does not yet allow real-time monitoring. It does not take into account the anatomical modifications undergone by the brain during the operation.

Today, thanks to the improvement of existing techniques, radiotherapy is open to patients who would not have been able to benefit from it a few years ago. This is the case with stereotactic radiotherapy. More targeted and less invasive, this technology, delivered in a few centers in France, has proven itself.

### *1.3. Brain tumor segmentation algorithms*

As reported in [16], brain tumor segmentation algorithms can be grouped into three main categories: conventional techniques, classification and clustering techniques, and deformable model techniques [17−18]. Threshold-based techniques, which compare pixel intensity to one or more intensity thresholds, belong to the first category of conventional techniques [19−20]. For example, an Otsu thresholding approach combined with some morphological operations (i.e., dilation and erosion) was proposed in [21] to detect brain tumor diseases from MRI images. An extended method that gives more accurate thresholding performance was proposed in [22]. In addition, region-based techniques, in which disjoint regions are formed by merging neighboring pixels based on a similarity criterion, are also classified in the first category [23]. These techniques include region-growth and watershed segmentation techniques. For example, an adaptive region-growing approach was proposed in [24] to solve the problem of manual threshold selection and weakness against noise; this approach is based on the variances and gradients of the inter and intra boundary curves. In another work [25], the authors presented a region growth approach based on a fixed threshold value for MRI segmentation, enhanced by an efficient preprocessing framework.

Classification and clustering techniques that form the second class are divided into supervised, semi-supervised, and unsupervised algorithms [26]. Many proven techniques belong to this class, such as K-means, support vector machines (SVMs), Markov random fields, artificial neural networks, convolutional neural networks (CNNs), and fuzzy C-means. For example, an SVM classification scheme combined with a kernel-space feature selection methodology was proposed in [27] for brain tumor segmentation. An unsupervised framework based on random forests was proposed in [28] to extract the tumor location, followed by a pattern classification phase. 86 features were used to create a training dataset to be presented as input to the classifier to define the tumor area. A fully supervised system for brain tumor segmentation based on a CNN architecture that exploits local and global contextual features was proposed in [29]. In a recently published paper [30], fast convolutional neural networks (FCNNs) are used to train, classify, and distinguish tumor from non-tumor patterns; training focused on patches and slices of axial, coronal, and sagittal brain views.

The third class consists of deformable model techniques, including parametric and geometric deformable models. These techniques have been proposed, among other things, to support intuitive interaction and high variability of mechanisms. Metaheuristic techniques have also been used for brain tumor segmentation, exploiting their ability to solve challenging optimization problems in the minimal time while avoiding local optima. Several techniques for brain tumor segmentation based on metaheuristics have been reported in the literature [31−32]. In [31], the Cuckoo search algorithm, an efficient optimization model, was applied to brain tumor segmentation from MRI images. Ant colony optimization metaheuristic and a fuzzy classification approach were combined in [32] to segment and extract the suspicious region from the brain MRI image containing the tumor position. In a recent paper [6], the authors proposed a novel region of interest (ROI) based brain tumor segmentation method. The region of interest was first identified using grid decomposition, and then only the region of interest was segmented using the spectral clustering method. Segmenting the brain tumor from a region of interest rather than from the entire image is an attractive concept. Nevertheless, this approach is limited by the increased

Preprints (www.preprints.org) | NOT PEER-REVIEWED | Posted: 14 July 2022 doi:10.20944/preprints202207.0211.v1

computational complexity resulting from the ROI identification step. In this study, we performed an analysis of variance (ANOVA) on the data to quantify the differences between the results. ANOVA is a statistical method generally used to assess the similarity of means in different groups by comparing variances [33−34]. The main advantages of ANOVA over other statistical methods lie in the following four points:

1. It is easy to implement using simple algebra.
2. It can be used to compare more than two samples.
3. It can be applied to groups with different numbers of observations.
4. It has been widely used and proven effective in various research fields such as agriculture, pharmacology, medicine and industry.

### *1.4. Main contributions*

This paper proposes an original brain tumor segmentation method based on the particle swarm optimization (PSO) technique that uses fixed two-way ANOVA as the fitness function. The proposed algorithm consists of three main steps:

1. The first step is to remove the skull bones from the image to eliminate unnecessary information.
2. In the second step, which is the main contribution of this study, the PSO technique is applied to detect the brain image block that contains the lesion. The two-way fixed ANOVA technique uses a fitness function to determine the best among all candidate blocks. All image blocks are tested, and the one that gives the minimum variance is considered. To overcome the computational complexity, PSO is used as a metaheuristic technique that identifies the best block in minimum time. The choice of PSO is based on the high performance of this optimization technique when applied to many real world applications. Therefore, the problem is posed as a maximization of a fitness function, and the well-known ANOVA method was chosen to measure the variance between the candidate block and the non-diseased block.
3. In the last step, K-means clustering, an efficient and simple partitioning technique is applied to the lesion block to classify it as tumor or non-tumor.

To illustrate the essential role of ANOVA in the proposed algorithm, the experimental results obtained with the ANOVA-based fitness function are compared to those obtained with the well-known dissimilarity criterion, the sum of absolute differences (SAD). The results of the comparison, using a database provided by the Kouba Imaging Center in Algiers (Algeria), demonstrate the efficiency and robustness of ANOVA.

The remainder of the paper is organized as follows. Section 2 presents the background of the method we propose here. In Section 3, the proposed algorithm is presented in detail, as well as the reasons for using PSO and ANOVA as the underlying techniques. Experimental results are presented in Section 4, and a conclusion summarizing the work is given in Section 5.

## 2. Review of the Background of the Proposed Approach

The proposed algorithm uses different methods to segment the brain tumor image. The PSO metaheuristic technique is applied to identify the ROI, and the fitness function that determines the best block that can be considered as ROI is based on ANOVA. Finally, the K-means method is used to segment the ROI. This section presents the main concepts of these methods in detail.

### *2.1. Particle Swarm Optimization*

Metaheuristic techniques have been developed to solve complex optimization problems when mathematical techniques fail or require high computational time. The process of any metaheuristic technique starts with one or more random solutions initialized in the search space. Then, powerful tools inspired by natural phenomena are used to iteratively

Preprints (www.preprints.org) | NOT PEER-REVIEWED | Posted: 14 July 2022 doi:10.20944/preprints202207.0211.v1

converge the solution(s) to the optimal solution. The success of a metaheuristic technique relies on its ability to explore the search space in depth and to exploit promising areas.

Metaheuristics are grouped into three categories based on the type of inspired natural phenomenon: (1) Evolutionary algorithms inspired by genetic inheritance for survival such as genetic algorithms (GAs) [35]; (2) Swarm intelligence that mimics the social behavior of a group of animals such as particle swarm optimization (PSO) [36]; and (3) Physics-based techniques, which are based on some physical rules such as simulated annealing (SA) [37]. Among the many metaheuristics developed in the literature, PSO has proven its efficiency in many applications [38−39].

PSO is a swarm intelligence technique proposed by Eberhart and Kennedy in 1995 [36], inspired by the flight behavior of birds. It has been successfully used in many application areas due to its simplicity of implementation and effectiveness.

In PSO, many particles or candidate solutions are randomly initialized in the search space, and then each particle iteratively adjusts its position according to its own and its colleagues' flight experience [36, 40−41]. The fundamental concept of PSO is to initialize $N_p$ candidate solutions randomly in the search space. Their velocities and positions are then updated using (1) and (2).

$$V_i = \omega \times V_i + c_1 \times R_1 \times (P_i - X_i) + c_2 \times R_2 \times (G - X_i) \quad (1)$$

$$X_i = X_i + V_i \quad (2)$$

Where $V_i$ and $X_i$ are the velocity and position of particle $i$, $P_i$ and $G$ are the individuals and global solutions, $R_1$ and $R_2$ are two random numbers, and $\omega$, $c_1$, and $c_2$ are the weights of physical, cognitive, and social influences, respectively; they control the exploration and exploitation phases in PSO.

Each candidate solution is evaluated through a fitness function. The individual and global best candidate solutions are updated based on the fitness function values.

A pseudo-code of PSO is described in Algorithm 1.

**Algorithm 1** PSO algorithm

1: Initialize the total number of candidate solutions $N_p$, and the maximum number of iterations $t_{max}$
2: Random initialization of candidate solutions
3: **for** $t = 1 : t_{max}$ **do**
4: Update the velocities $V$ with (1)
5: Update the positions $X$ with (2)
6: Evaluate the positions $X$ with the fitness function
7: Update the individual ($P_i$) and global ($G$) solutions
8: **End for**

*2.2. Analysis of Variance (ANOVA)*

Analysis of variance (ANOVA) is a statistical method developed by Larson in 2008 [33] to analyze the variation of a response variable determined under different conditions defined by discrete factors. More precisely, the principle of ANOVA is to determine, using a statistical test, whether the share of dispersion attributable to the factor under study is significantly greater than the residual share. If the factorial dispersion is significantly larger than the residual dispersion, it means that the dispersion of the data around the means of each modality is small compared to the dispersion of the means around the overall mean. In this case, if the means relative to each modality are highly dispersed, while the intra-class variability is low, it means that the means are globally different. Con-

Preprints (www.preprints.org) | NOT PEER-REVIEWED | Posted: 14 July 2022 doi:10.20944/preprints202207.0211.v1

versely, if the factorial dispersion is of the same order of magnitude as the residual dispersion, it means that the means are not different overall. Finally, the ANOVA is used to test the equality of the means of the different groups by comparing their variances.

The ANOVA technique has two models that we will detail: the one-way fixed-effects ANOVA and the two-way fixed-effects ANOVA [34].

2.2.1. One-way fixed-effects ANOVA

The results of a one-way ANOVA are only significant if the following three assumptions are met:

- Each sample comes from a normally distributed population.
- The variances of the populations from which the samples come are equal.
- The observations in each group are independent of each other, and the observations in the groups were obtained by random sampling.

The null and alternative hypotheses defined in a one-way ANOVA are as follows:

- Null hypothesis or $H_0$: The means of the $k$ groups in the study population are equal.
- Alternative hypothesis or $H_1$: At least one group means differs from the others.

A statistical test, for example Fisher's $F$ test with $(k-1)$ [factorial part] and $(N-k)$ [residual part, where $N$ is the size of the study population] degrees of freedom (provided that the normality and homogeneity of the residuals are respected), at a given $\alpha$ risk (generally 5%), allows to reject or not the null hypothesis. The key elements of the one-way ANOVA method are summarized in Table 1. The main definitions associated with this table are defined below:

- The total sum of squares ($SST$) is the sum of the squared distances between each observed value and the overall mean. It is the sum of a weight attributable to the factor ($SSF$) and a weight attributable to the residues ($SSE$). It can therefore be summarized by (3).
- The factorial sum of squares ($SSF$), which measures the differences between the group averages and the overall average, is defined in (4).
- The residual sum of squares ($SSR$) is defined in (5).
- $p$ is the $p$-value that corresponds to $F_{k-1,N-k}$.

Ultimately, if the $p$-value is less than the threshold value that has been defined (usually 5%), then the null hypothesis can be rejected, which implies in this case that at least one of the means in a population group is different from the others.

$$SST = SSF + SSE = \sum_{i=1}^{k}\sum_{j=1}^{n_j}\left(y_{ij} - \bar{y}\right)^2 \quad (3)$$

- $SSF$: factorial sum of squares.
- $SSE$: error sum of squares.
- $i$: index of the modalities (groups), i.e., from 1 to $k$.
- $j$: observation index in a modality.
- $y_{ij}$: observations.
- $\bar{y}$: overall mean of observations.

Preprints (www.preprints.org) | NOT PEER-REVIEWED | Posted: 14 July 2022 doi:10.20944/preprints202207.0211.v1

$$SSF = \sum_{i=1}^{k} n_i(\overline{y_i} - \bar{y})^2 \quad (4)$$

- $n_i$: number of data for each of the modalities.
- $\overline{y_i}$: mean of the $n_i$-values of the considered modality.

$$SSR = \sum_{i=1}^{k} \sum_{j=1}^{n_j} (y_{ij} - \overline{y_i})^2 \quad (5)$$

**Table 1.** Key elements of one-way ANOVA calculations.

| Source of variation | Sum of squares | Degrees of freedom | Mean squares | *F*-value | *p*-value |
|---|---|---|---|---|---|
| Factor | $SSF$ (attributable to factor) | $k-1$ | $\frac{SSF}{k-1}$ | | |
| Residues or error | $SSE$ (attributable to residues) | $N-k$ | $\frac{SSE}{N-k}$ | $F_{k-1,N-k} = \frac{\frac{SSF}{k-1}}{\frac{SSE}{N-k}}$ | $p$ |
| Total | $SST = SSF + SSE$ | $N-1$ | | | |

2.2.2. Two-way fixed-effects ANOVA

The principle of the two-way fixed effects ANOVA model is, first, to decompose the total dispersion of the data into four sources: the contribution attributable to the first factor noted $A$; the contribution attributable to the second factor noted $B$; the contribution attributable to the interaction of the two factors; and the unexplained or residual share. In this method, each level of a factor is combined with the other factor: the two factors are said to be crossed. Then, in a second step, it is necessary to evaluate, with the help of a statistical test, if the factorial shares, and the one linked to the interaction, are significantly higher than the residual share.

Before going into the details of the method, it is necessary to define the following parameters:

- The first categorical variable studied (often called factor $A$) has $a$ modalities (we also say that the factor $A$ contains $a$ levels). The index of the modalities of this first categorical variable, noted $i$, goes from 1 to $a$. Similarly, the second categorical variable studied (often called factor $B$) has $b$ modalities. The index of the modalities of this first categorical variable, noted $i$, goes from 1 to $b$.
- The total number of observations is always noted $N$, but the number of observations in each cell of the factorial design is noted $n_{ij}$. Equation (6) defines the relationship between $N$ and $n_{ij}$. In the following, $n$ is the number of repetitions.
- The observations in each cell of the factorial design (i.e., in each factorial combination), are denoted by $y_{ijk}$ where $k$ is the index of the replication in each crossover. The overall average of the responses is defined in (7), where the two points ("..") correspond to the indices of the first and second categorical variables.
- The means of each cross of modalities are noted $\overline{y_{ij}}$ (see (8)).
- The marginal means of the modalities of the first variable and those of the second variable are respectively noted $\overline{y_{i.}}$ and $\overline{y_{.j}}$ and meet the definitions of equations (9) and (10).
- The marginal numbers of the modalities of the first variable and those of the second variable are respectively noted $n_{i.}$ and $n_{.j}$ and meet the definitions of equations (11) and (12).

Preprints (www.preprints.org) | NOT PEER-REVIEWED | Posted: 14 July 2022 doi:10.20944/preprints202207.0211.v1

$$N = \sum_{i=1}^{a}\sum_{j=1}^{b} n_{ij} \tag{6}$$

$$\bar{y}_{..} = \frac{1}{N}\sum_{i=1}^{a}\sum_{j=1}^{b}\sum_{k=1}^{n_{ij}} y_{ijk} \tag{7}$$

$$\overline{y_{ij}} = \frac{1}{n_{ij}}\sum_{k=1}^{n_{ij}} y_{ijk} \tag{8}$$

$$\bar{y}_{i\cdot} = \frac{1}{b}\sum_{j=1}^{b} \overline{y_{ij}} \tag{9}$$

$$\overline{y_{\cdot j}} = \frac{1}{a}\sum_{i=1}^{a} \overline{y_{ij}} \tag{10}$$

$$n_{i\cdot} = \sum_{j=1}^{b} n_{ij} \tag{11}$$

$$n_{\cdot j} = \sum_{i=1}^{a} n_{ij} \tag{12}$$

Like the one-way ANOVA method and as shown in Table 2, the two-way ANOVA technique first measures the total dispersion of the data by calculating the total sum of squares ($SST$) as defined in (13). Then, the total dispersion is decomposed into the part attributable to the first factor noted $SSA$ (see (14)), the part attributable to the second factor noted $SSB$ (see (15)), the part attributable to the interaction between the two factors noted $SSAB$ (see (16)), and finally the part attributable to the residues noted $SSR$ (see (17)). After calculating the variances of the factors, interaction and residuals, which are referred to as mean squares in Table 2, statistical hypothesis tests, i.e., $F$-tests of the ratio of two variances, are performed to assess whether each of the three variance shares is significantly greater than the residual variance. Under the assumptions of normality and homogeneity of residuals, the $F$-test statistic follows a Fisher distribution with:

- $(a-1)$ and $ab(n-1)$ degrees of freedom for the tests related to factor $A$;
- $(b-1)$ and $ab(n-1)$ degrees of freedom for the tests related to factor $B$;
- $(a-1)(b-1)$ and $ab(n-1)$ degrees of freedom for the tests related to the interaction between the two factors $A$ and $B$.

Finally, as in the previous section and in the classical way, we must calculate the probability, under the null hypothesis $H_0$, of observing such an $F$-value: this is the $p$-value. This $p$-value is compared to the chosen level of significance (generally set at 5%). If the $p$-value is lower than the significance level, we conclude that the effect is significant. If not, the conclusion is not that there is no effect, but that there is no evidence of an effect. It is possible, for example, that the sample sizes are too small to show a significant difference.

$$SST = \sum_{i=1}^{a}\sum_{j=1}^{b}\sum_{k=1}^{n_{ij}} \left(y_{ijk} - \bar{y}_{..}\right)^2 \tag{13}$$

$$SSA = bn\sum_{i=1}^{a} \left(\bar{y}_{i\cdot} - \bar{y}_{..}\right)^2 \tag{14}$$

Preprints (www.preprints.org) | NOT PEER-REVIEWED | Posted: 14 July 2022 doi:10.20944/preprints202207.0211.v1

$$SSB = an\sum_{j=1}^{b}\left(\overline{y_{.j}} - \overline{y_{..}}\right)^2 \tag{15}$$

$$SSAB = \sum_{i=1}^{a}\sum_{j=1}^{b} n\left(\overline{y_{ij}} - \overline{y_{..}}\right)^2 - SSA - SSB \tag{16}$$

$$SSR = \sum_{i=1}^{a}\sum_{j=1}^{b}\left(y_{ijk} - \overline{y_{ij}}\right)^2 \tag{17}$$

**Table 2.** Key elements of two-way ANOVA calculations.

| Source of variation | Sum of squares | Degrees of freedom | Mean squares | *F*-value | *p*-value |
|---|---|---|---|---|---|
| Factor $A$ | $SSA$ (attributable to factor $A$) | $a-1$ | $\frac{SSA}{a-1}$ | $F_{A(a-1,ab(n-1))} = \frac{\frac{SSA}{a-1}}{\frac{SSE}{ab(n-1)}}$ | $p_A$ |
| Factor $B$ | $SSB$ (attributable to factor $B$) | $b-1$ | $\frac{SSB}{b-1}$ | $F_{B(b-1,ab(n-1))} = \frac{\frac{SSB}{b-1}}{\frac{SSE}{ab(n-1)}}$ | $p_B$ |
| Interaction $AB$ | $SSAB$ (attributable to interaction A$B$) | $(a-1)(b-1)$ | $\frac{SSAB}{(a-1)(b-1)}$ | $F_{AB((a-1)(b-1),ab(n-1))} = \frac{\frac{SSAB}{(a-1)(b-1)}}{\frac{SSE}{ab(n-1)}}$ | $p_{AB}$ |
| Residues or error | $SSE$ (attributable to residues) | $ab(n-1)$ | $\frac{SSE}{ab(n-1)}$ | $F$ | $p$ |

*2.3. K-means clustering technique*

K-means is an unsupervised clustering technique that separates all data into k clusters. Each data point is assigned to one of the K clusters that minimize the Euclidean distance between the data point and the cluster's center. The centers are then updated, and the data points are reassigned to the closest center throughout several iterations. The iterations are repeated until the centers do not move or the data points do not change the cluster to which they are assigned [42-43]. Algorithm 2 describes the K-means clustering technique.

**Algorithm 2.** K-means Algorithm

1: Initialize the number of clusters
2: Choose initial cluster centers
3: **While** The stopping criterion is not satisfied, **do**
4: Assign each data point to one cluster
5: Update the center of each cluster
6: **End while**

Preprints (www.preprints.org) | NOT PEER-REVIEWED | Posted: 14 July 2022 doi:10.20944/preprints202207.0211.v1

## 3. Proposed Segmentation Method

The proposed segmentation method consists of three main stages. In the first stage, a pre-processing of the image is performed to eliminate any unnecessary data. Then, PSO is applied to identify the ROI, and K-means is used to segment the ROI. An illustrative diagram is shown in Figure 2, and a simple flowchart of the proposed method is presented in Figure 3.

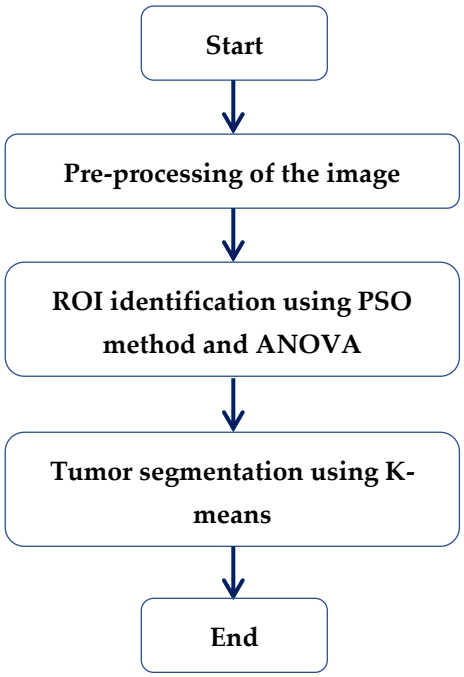


**Figure 2.** Diagram of the proposed approach.

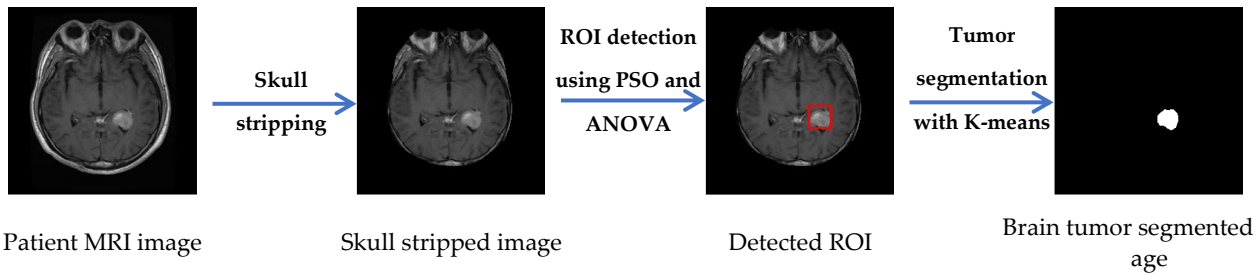


**Figure 3.** Flowchart of the proposed segmentation method.

### *3.1. Image Preprocessing*

Image preprocessing is vital in removing noisy, inconsistent, incomplete, and irrelevant data. Several approaches are possible to improve the quality of the image during its transmission or storage [44]. We will mention, for example, those based on the concept of compressed sensing where the enhancement of the image is carried out during acquisition [45−49]. An alternative approach is to perform a simple and efficient denoising (close to optimality) from 1st or 2nd generation wavelets [50−52].

Skull stripping is a crucial step to eliminate from the brain image all non-brain tissues such as skull's bone, fat, skin, etc. [53]. For this purpose, several approaches have been developed [54−55]. The first step of the proposed technique is a skull stripping procedure in which the greyscale image is converted into a binary image using a fixed threshold. Then two morphological operations, filling and erosion, are applied to the binary image.

Preprints (www.preprints.org) | NOT PEER-REVIEWED | Posted: 14 July 2022 doi:10.20944/preprints202207.0211.v1

Finally, the original image is masked by the obtained binary image; the generated image is the skull-stripped image (see Figure 4) [42, 56−57].

*3.2. ROI Detection*

PSO is a powerful metaheuristic technique designed to solve complex optimization problems. The proposed algorithm uses PSO to search for the optimal block containing the tumor within the MRI image. The principal concept of this stage is described in the following.

First, several candidate blocks are initialized randomly within the MRI image, and each candidate block is evaluated with a fitness function to determine the best blocks (see Figure 5). The proposed algorithm's fitness function is based on the two-way ANOVA to analyze variance. The used data are the candidate block and the MRI image of a no-disease brain. The used fitness function is given by (18).

$$fitness = \frac{MSA}{MSE} + \frac{MSB}{MSE} \tag{18}$$

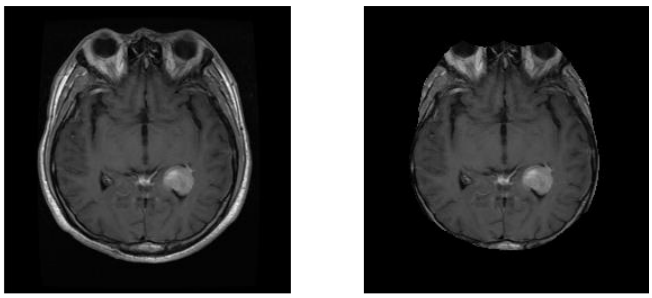

**(a)** Original brain image **(b)** Brain image after preprocessing

**Figure 4.** Preprocessing step.

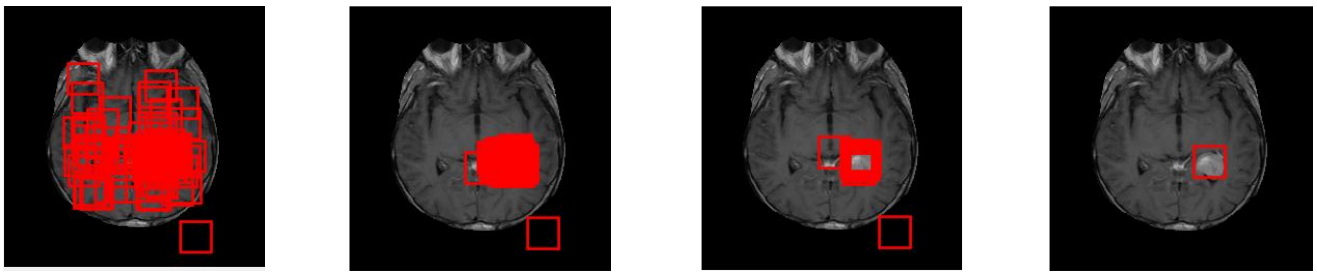

**(a)** Candidate blocks after 5 iterations **(b)** Candidate blocks after 15 iterations **(c)** Candidate blocks after 35 iterations **(d)** Candidate blocks after 50 iterations

**Figure 5.** ROI identification using PSO and ANOVA.

Since MSA and MSB represent the variability among group means and MSE represents the variability within the group divided by the degree of freedom, the high values of MSA and MSB correspond to significant variability between the candidate block and the no-disease brain image, which means that there is an abnormal tissue in this block. In other words, the large variability between the candidate block and the no-disease brain image signifies that this candidate block contains a tumor. Therefore, the candidate block that corresponds to the fitness function's maximum value is considered the best block found. Once the fitness function evaluation and the global and individual best blocks have been updated, the positions of candidate blocks are also updated using (1) and (2). The fitness function evaluation and updating block processes are repeated until maximum iterations are reached. Since some solutions can be evaluated more than once in a metaheuristic technique, the fitness function value and the positions of each candidate solution are stored in a matrix to reduce the computational time. Then, if the PSO algorithm attempts

Preprints (www.preprints.org) | NOT PEER-REVIEWED | Posted: 14 July 2022 doi:10.20944/preprints202207.0211.v1

to evaluate an already evaluated solution, its fitness value is taken directly from the matrix. This idea has decreased computational complexity in block matching problems [58].

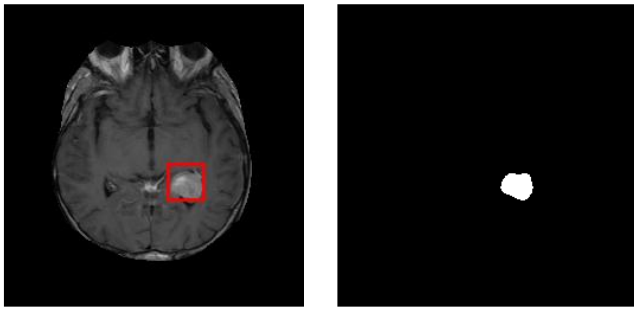

**(a)** Identified ROI **(b)** ROI segmented with K-means

**Figure 6.** ROI segmentation using K-means.

**(a)** Segmentation using our method **(b)** Ground truth

**Figure 7.** Performance comparison between the proposed brain tumor segmentation and ground truth.

### *3.3. Tumor Segmentation*

For tumor segmentation, the K-means clustering technique is applied to the global best block, found in the ROI detection stage, containing the tumor. Because we classify the blocks as tumor or non-tumor, the K-means method uses two clusters. Figure 6 illustrates the identified ROI and its segmentation using K-means.

The segmentation results are then evaluated by measuring the similarity or dissimilarity between them and the ground truth. Figure 7 illustrates the segmentation result of our approach and the ground truth.

Over the years, several similarity and dissimilarity metrics have been formulated and reported in the literature. To evaluate our algorithm, we used the following metrics [59]:

1. Dice similarity coefficient:

$$\frac{2TP}{2TP + FP + FN} \tag{19}$$

2. Jaccard distance:

$$\frac{TP}{TP + FP + FN} \tag{20}$$

3. Correlation coefficient:

$$\frac{1}{M \times N} \sum_{i=1}^{M} \sum_{j=1}^{N} \left( \frac{Is_{i,j} - Is}{\sigma_{Is}} \right) \left( \frac{Ig_{i,j} - Ig}{\sigma_{Ig}} \right) \tag{21}$$

4. Mean Squared Error (MSE):

$$\frac{1}{M \times N} \sum_{i=1}^{M} \sum_{j=1}^{N} (Is_{i,j} - Ig_{i,j})^2 \tag{22}$$

Preprints (www.preprints.org) | NOT PEER-REVIEWED | Posted: 14 July 2022 doi:10.20944/preprints202207.0211.v1

where $FP$ is the number of false positives, $TP$ is the number of true positives, $FN$ is the number of false negatives, $Is$ refers to the segmented image with our technique, $Ig$ is the ground truth image, $M$ and $N$ represent the image's size.

Since the Dice coefficient and Jaccard distance are two metrics of similarity, a powerful method should maximize these criteria. The correlation criterion is also a similarity metric and varies between $-1$ and $+1$; the perfect positive correlation is achieved when the coefficient equals $+1$. MSE is, on the other hand, a dissimilarity metric; the minimum value of MSE is indicative of a robust segmentation technique [60].

## 4. Experimental Analysis

The proposed algorithm is implemented for the evaluation study on different MRI images and a ground truth obtained from a database provided by the Center of Imaging in Kouba (CIKA, Algeria) [61], which includes the brain tumor images and the corresponding ground truth images. The disease-free brain images used are in DICOM format and selected in the same sections as the brain tumor images.

This section is divided into two parts. The first part illustrates the essential role of ANOVA in our algorithm. The results obtained using the ANOVA-based fitness function are compared to those obtained with the SAD fitness function. Following the same concept of variability explained above, the candidate block that gives the maximum SAD value is considered as the tumor block. In the second part of this work, we compared the experimental results of our algorithm with several well-known segmentation techniques such as FCM, K-means, Otsu thresholding, local thresholding and Watershed segmentation..

### *4.1. Experiment #1*

The robustness of any technique based on metaheuristics depends on the fitness function used because this latter is a decisive parameter in evaluating all the candidate solutions and determining the optimal global solution. In our segmentation technique, the fitness function measures the variability or the difference between the candidate blocks in the brain tumor image and the corresponding blocks in the no-disease image; a significant difference between them indicates the existence of a tumor. We have resorted to the statistical method ANOVA, using the fitness function expressed in (18). Since the difference can also be measured with any dissimilarity criterion, we have changed the used fitness function of (18) and replaced it with the SAD criterion in order to prove the efficiency of our ANOVA-based fitness function. The SAD metric, also called the L1 norm or Manhattan norm, is a dissimilarity criterion used to compare the intensities of two blocks or images [60] and is defined as follows:

$$SAD = \sum_{i=1}^{M} \sum_{j=1}^{N} \left| I_{1_{i,j}} - I_{2_{i,j}} \right| \tag{23}$$

Where $I_1$ and $I_2$ represent the candidate blocks in the brain tumor image and the no-disease image.

A high SAD value shows a substantial difference between the candidate block and the no-disease image, indicating the presence of a tumor. Therefore, the candidate block that gives the maximum SAD value is considered the tumor block. Figure 8 shows the original images before and after the pre-processing and segmentation procedures, where the used fitness function is based on ANOVA and the SAD criterion.

Preprints (www.preprints.org) | NOT PEER-REVIEWED | Posted: 14 July 2022 doi:10.20944/preprints202207.0211.v1

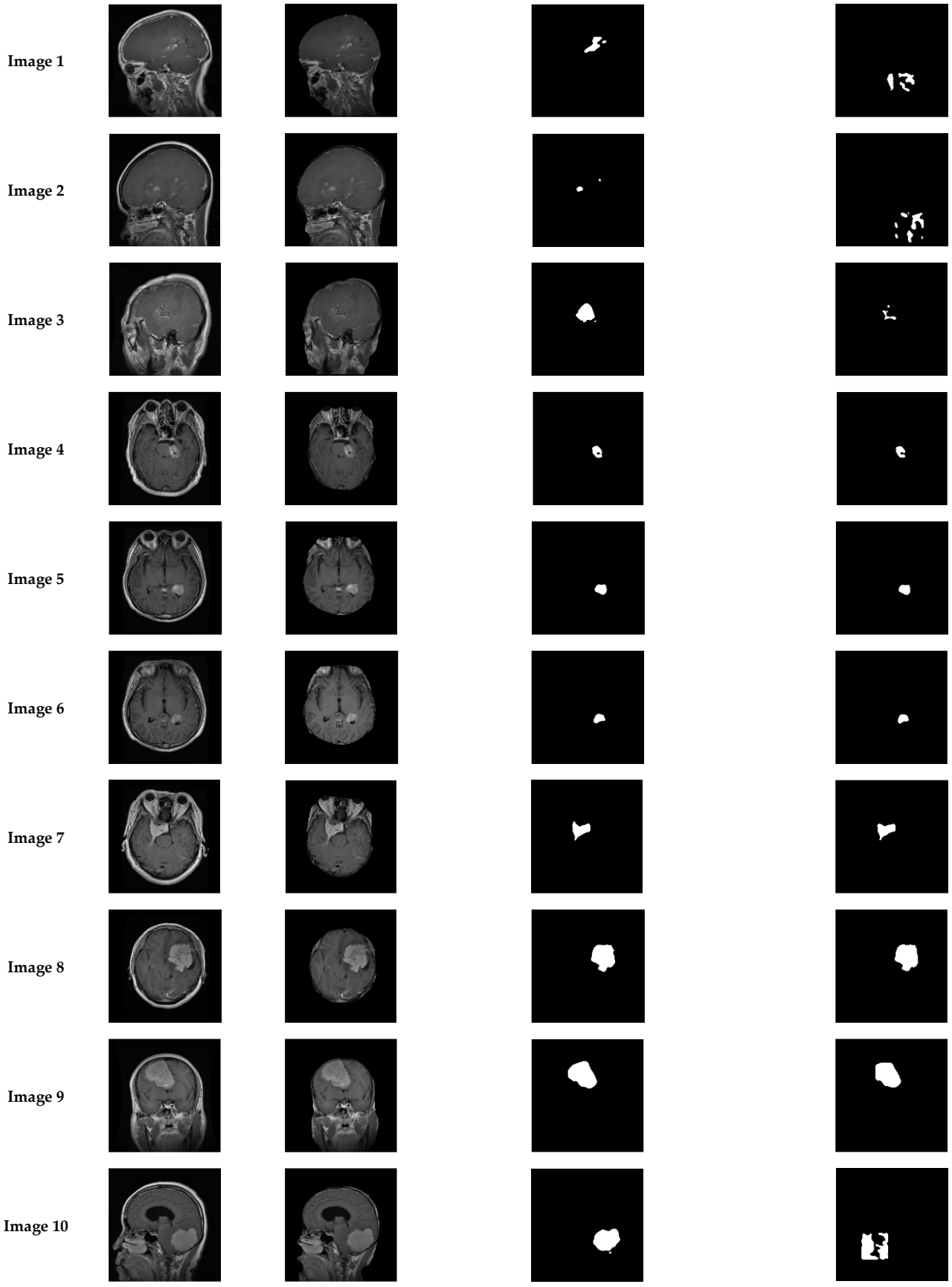


**(a)** Original images **(b)** Pre-processing **(c)** Our method based on ANOVA **(d)** Our method based on SAD

**Figure 8.** Efficiency of brain tumor segmentation: comparison of ANOVA and SAD-based methods.

Preprints (www.preprints.org) | NOT PEER-REVIEWED | Posted: 14 July 2022 doi:10.20944/preprints202207.0211.v1

Tables 3, 4, 5, and 6 show the Dice, Jaccard, correlation, and MSE values obtained by our segmentation method with the two fitness functions tested. From the comparison of the results, it is clear that using ANOVA as a fitness function yields much better results than those obtained with the SAD fitness function, demonstrating the robustness and effectiveness of the technique in evaluating candidate blocks.

**Table 3.** The results of our segmentation method using the Dice similarity coefficient with two fitness functions: ANOVA and SAD.

| Images | Our method based on ANOVA | Our method based on SAD |
|---|---|---|
| Image 1 | 62.008% | Non-relevant segmentation |
| Image 2 | 78.997% | Non-relevant segmentation |
| Image 3 | 73.276% | 24.432% |
| Image 4 | 83.265% | 78.242% |
| Image 5 | 88.252% | 87.581% |
| Image 6 | 87.844% | 85.748% |
| Image 7 | 91.919% | 88.809% |
| Image 8 | 94.535% | 93.593% |
| Image 9 | 96.211% | 90.469% |
| Image 10 | 95.154% | Non-relevant segmentation |

**Table 4.** The results of our segmentation method using the Jaccard distance with two fitness functions: ANOVA and SAD.

| Images | Our method based on ANOVA | Our method based on SAD |
|---|---|---|
| Image 1 | 44.936% | Non-relevant segmentation |
| Image 2 | 65.285% | Non-relevant segmentation |
| Image 3 | 57.823% | 13.916% |
| Image 4 | 71.329% | 64.26% |
| Image 5 | 78.974% | 77.907% |
| Image 6 | 78.323% | 75.051% |
| Image 7 | 85.046% | 79.871% |
| Image 8 | 89.637% | 87.959% |
| Image 9 | 92.699% | 82.598% |
| Image 10 | 90.756% | Non-relevant segmentation |

Preprints (www.preprints.org) | NOT PEER-REVIEWED | Posted: 14 July 2022 doi:10.20944/preprints202207.0211.v1

**Table 5.** The results of our segmentation method using the Correlation coefficient with two fitness functions: ANOVA and SAD.

| Images | Our method based on ANOVA | Our method based on SAD |
|---|---|---|
| Image 1 | 0.673064 | 0.475478 |
| Image 2 | 0.790116 | 0.386167 |
| Image 3 | 0.761069 | 0.532032 |
| Image 4 | 0.870553 | 0.820469 |
| Image 5 | 0.897922 | 0.888510 |
| Image 6 | 0.891440 | 0.865518 |
| Image 7 | 0.925806 | 0.903027 |
| Image 8 | 0.952524 | 0.942536 |
| Image 9 | 0.953663 | 0.66343 |
| Image 10 | 0.950669 | 0.94286 |

**Table 6.** The results of our segmentation method using the MSE metric with two fitness functions: ANOVA and SAD.

| Images | Our method based on ANOVA | Our method based on SAD |
|---|---|---|
| Image 1 | 0.0006647 | 0.0010605 |
| Image 2 | 0.0000158 | 0.0014934 |
| Image 3 | 0.0003579 | 0.0005049 |
| Image 4 | 0.0000657 | 0.0001091 |
| Image 5 | 0.0000398 | 0.0000464 |
| Image 6 | 0.0000243 | 0.0000361 |
| Image 7 | 0.0000686 | 0.0001325 |
| Image 8 | 0.0001223 | 0.0002402 |
| Image 9 | 0.0000498 | 0.0004337 |
| Image 10 | 0.0000414 | 0.0133088 |

### *4.2. Experiment #2*

We assessed our algorithm's effectiveness against several well-known segmentation techniques in the second experiment. The segmented images obtained with our method and other segmentation methods are shown in Figure 9. Besides, we can see from the statistical comparisons highlighted in Tables 7-10 that the proposed method can segment the brain tumor very efficiently. The first stage of our algorithm that determines the ROI then segments only this region, making the brain tumor segmentation results free of any irrelevant information, such as skull's bone, as opposed to other segmentation techniques, such as those based on Otsu or local thresholding in which some of the extraneous information remains on the segmented image.

Preprints (www.preprints.org) | NOT PEER-REVIEWED | Posted: 14 July 2022 doi:10.20944/preprints202207.0211.v1

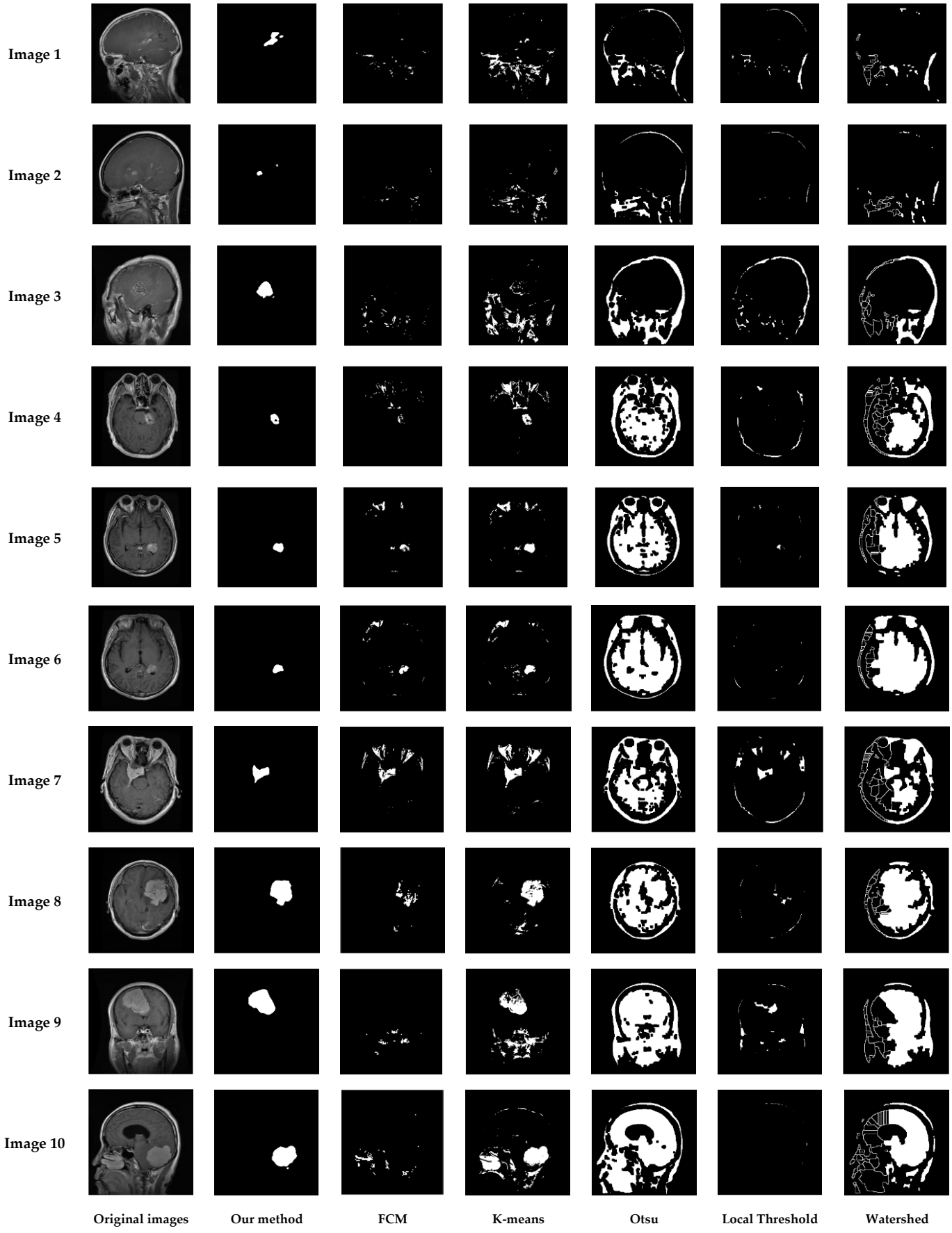


**Figure 9.** Efficiency of brain tumor segmentation: comparison between the proposed ANOVA-based method and other well-known methods.

Preprints (www.preprints.org) | NOT PEER-REVIEWED | Posted: 14 July 2022 doi:10.20944/preprints202207.0211.v1

**Table 7.** Comparison between the results of our segmentation method with some well-known segmentation techniques using the Dice similarity coefficient.

| Images | Our method | FCM | K-means | Otsu thresholding | Local thresholding | Watershed thresholding |
|---|---|---|---|---|---|---|
| Image 1 | 62.008% | 2.9106% | 6.858% | 0.044% | 0.303% | Non-relevant segmentation |
| Image 2 | 78.997% | Non-relevant segmentation | Non-relevant segmentation | Non-relevant segmentation | Non-relevant segmentation | Non-relevant segmentation |
| Image 3 | 73.276% | 1.127% | 6.690% | Non-relevant segmentation | Non-relevant segmentation | Non-relevant segmentation |
| Image 4 | 83.265% | 25.948% | 24.823% | 5.750% | 0.906% | 8.297% |
| Image 5 | 88.252% | 38.213% | 38.137% | 6.130% | 20.762% | 7.738% |
| Image 6 | 87.844% | 42.716% | 35.910% | 4.683% | 4.088% | 5.357% |
| Image 7 | 91.919% | 44.635% | 40.291% | 10.921% | 35.751% | 13.968% |
| Image 8 | 94.535% | 50.052% | 79.763% | 25.940% | 11.712% | 27.638% |
| Image 9 | 96.211% | 1.476% | 56.53% | 25.038% | 23.014% | 25.643% |
| Image 10 | 95.154% | 0.810% | 48.957% | 18.878% | Non-relevant segmentation | 28.530% |

**Table 8.** Comparison between the results of our segmentation method with some well-known segmentation techniques using the Jaccard distance.

| Images | Our method | FCM | K-means | Otsu thresholding | Local thresholding | Watershed thresholding |
|---|---|---|---|---|---|---|
| Image 1 | 44.936% | 1.4768% | 3.551% | 0.022% | 0.151% | Non-relevant segmentation |
| Image 2 | 65.285% | Non-relevant segmentation | Non-relevant segmentation | Non-relevant segmentation | Non-relevant segmentation | Non-relevant segmentation |
| Image 3 | 57.823% | 0.566% | 3.461% | Non-relevant segmentation | Non-relevant segmentation | Non-relevant segmentation |
| Image 4 | 71.329% | 14.908% | 14.17% | 2.96% | 0.455% | 4.328% |
| Image 5 | 78.974% | 23.619% | 23.561% | 3.161% | 11.583% | 4.025% |
| Image 6 | 78.323% | 27.159% | 21.885% | 2.398% | 2.087% | 2.752% |
| Image 7 | 85.046% | 28.729% | 25.228% | 5.776% | 21.766% | 7.508% |
| Image 8 | 89.637% | 33.38% | 66.339% | 14.903% | 6.220% | 16.035% |
| Image 9 | 92.699% | 0.7438% | 39.402% | 14.310% | 13.003% | 14.707% |
| Image 10 | 90.756% | 0.406% | 32.413% | 10.423% | Non-relevant segmentation | 16.639% |

Preprints (www.preprints.org) | NOT PEER-REVIEWED | Posted: 14 July 2022 doi:10.20944/preprints202207.0211.v1

**Table 9.** Comparison between the results of our segmentation method with some well-known segmentation techniques using the Correlation coefficient.

| Images | Our method | FCM | K-means | Otsu thresholding | Local thresholding | Watershed thresholding |
|---|---|---|---|---|---|---|
| Image 1 | 0.673064 | 0.157563 | 0.293867 | 0.275414 | 0.196262 | 0.214095 |
| Image 2 | 0.790116 | 0.239039 | 0.250315 | 0.219895 | 0.138782 | 0.160484 |
| Image 3 | 0.761069 | 0.182389 | 0.253495 | 0.243609 | 0.129738 | 0.243366 |
| Image 4 | 0.870553 | 0.289513 | 0.417104 | 0.159479 | 0.175391 | 0.192943 |
| Image 5 | 0.897922 | 0.378542 | 0.561895 | 0.164128 | 0.249723 | 0.177235 |
| Image 6 | 0.891440 | 0.502674 | 0.557390 | 0.135842 | 0.154660 | 0.142385 |
| Image 7 | 0.925806 | 0.537026 | 0.560681 | 0.224682 | 0.356487 | 0.281344 |
| Image 8 | 0.952524 | 0.474860 | 0.822597 | 0.328776 | 0.188492 | 0.3892 |
| Image 9 | 0.966158 | 0.255578 | 0.593773 | 0.333411 | 0.236488 | 0.3951 |
| Image 10 | 0.953663 | 0.300080 | 0.602117 | 0.271452 | 0.084133 | 0.3824 |

**Table 10.** Comparison between the results of our segmentation method with some well-known segmentation techniques using the MSE metric.

| Images | Our method | FCM | K-means | Otsu thresholding | Local thresholding | Watershed thresholding |
|---|---|---|---|---|---|---|
| Image 1 | 0.0006647 | 0.0012972 | 0.0021345 | 0.0057836 | 0.0020789 | 0.0031144 |
| Image 2 | 0.0000158 | 0.0000920 | 0.0005815 | 0.0040139 | 0.0001327 | 0.0011636 |
| Image 3 | 0.0003579 | 0.0008458 | 0.0046264 | 0.0242370 | 0.0024103 | 0.0155236 |
| Image 4 | 0.0000657 | 0.0005798 | 0.0013554 | 0.0915980 | 0.0010545 | 0.0589136 |
| Image 5 | 0.0000399 | 0.0005223 | 0.0006572 | 0.0973590 | 0.0006525 | 0.0915326 |
| Image 6 | 0.0000243 | 0.0002296 | 0.0003564 | 0.1246628 | 0.0005443 | 0.1213210 |
| Image 7 | 0.0000686 | 0.0007301 | 0.0018533 | 0.0672948 | 0.0017184 | 0.0423277 |
| Image 8 | 0.0001223 | 0.0049038 | 0.0004566 | 0.0636407 | 0.0068672 | 0.0722 |
| Image 9 | 0.0000498 | 0.0073548 | 0.0018346 | 0.1033327 | 0.0065827 | 0.0887 |
| Image 10 | 0.0000414 | 0.0060980 | 0.0040885 | 0.1220065 | 0.0062485 | 0.0533 |

To complement the above results, Figures 10, 11, 12 and 13 further highlight the robustness and effectiveness of our proposed method. As shown in the graphs of Figures 10−13, the results of our algorithm (blue bars in each figure) are the highest in Dice, Jaccard, and Correlation and the lowest in MSE compared to other competing techniques,

Preprints (www.preprints.org) | NOT PEER-REVIEWED | Posted: 14 July 2022 doi:10.20944/preprints202207.0211.v1

which proves the efficiency and robustness of our method. Thus, all the experimental results demonstrate that the proposed method outperforms all other competing methods.

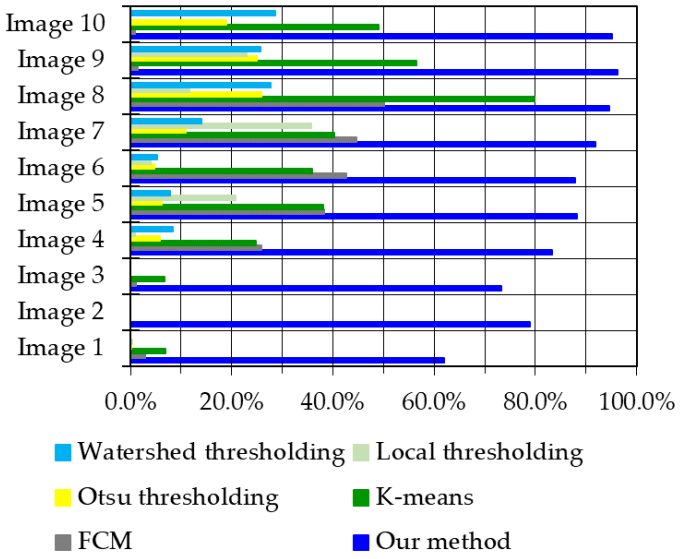


**Figure 10.** Comparison of segmentation results based on the Dice similarity coefficient.

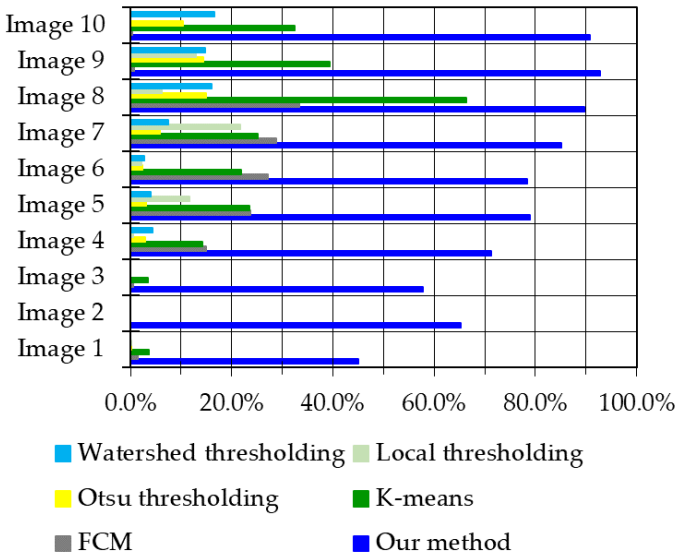


**Figure 11.** Comparison of segmentation results based on the Jaccard Distance.

Preprints (www.preprints.org) | NOT PEER-REVIEWED | Posted: 14 July 2022 doi:10.20944/preprints202207.0211.v1

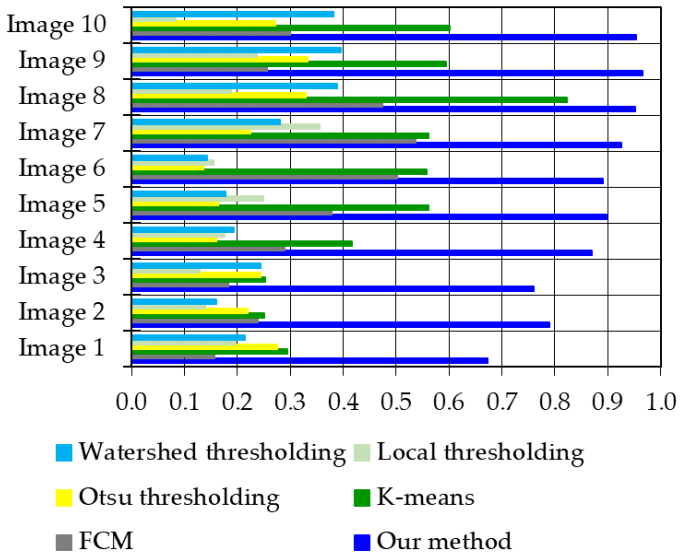


**Figure 12.** Comparison of segmentation results based on the correlation coefficient.

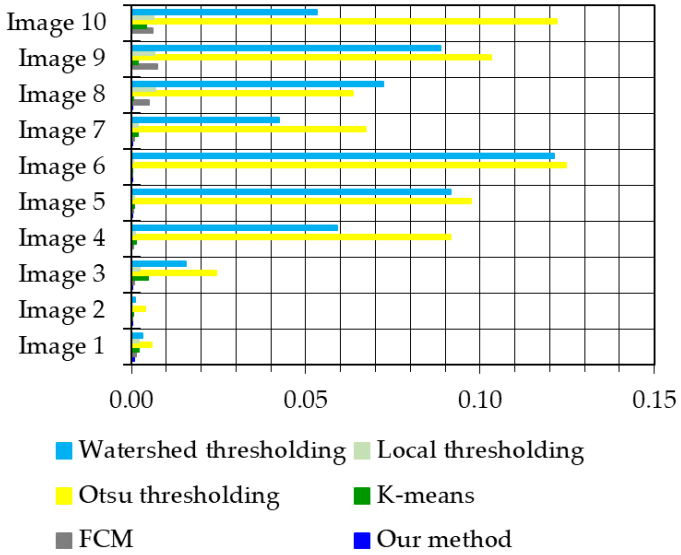


**Figure 13.** Comparison of segmentation results based on the MSE metric.

## 5. Conclusions

In this paper, a new method for brain tumor segmentation has been proposed. This method consists of four steps:

- The skull bone is precisely removed from the image to exclude irrelevant data.
- The particle swarm optimization (PSO) technique is then applied to detect the region of interest (ROI) that contains the brain lesion.
- The fitness function used to evaluate the candidate blocks is based on a two-way fixed-effects analysis of variance (ANOVA).
- Finally, in the last step of the method, the K-means segmentation method is used in the lesion block to classify it into two possible categories, tumor and non-tumor.

An evaluation study was performed using a large magnetic resonance imaging (MRI) database; a visual assessment and four statistical measures were used to evaluate the performance of tumor segmentation. A sample of 10 images representing the most clinically

encountered positions was used for the visual assessment. The results show that competing approaches do not provide usable segmentation results in some cases, whereas our approach is a promising solution for clinical decision support. Indeed, statistically the results show that the proposed method gives a tumor segmentation accuracy of 96%, outperforming other state-of-the-art methods.

In future work, we plan to further improve the performance of our study by targeting:

- Using generative adversarial networks [62−65] to preprocess, colorize, correct, and enhance images before presenting them to the segmentation algorithm.
- Combining the features extracted by the proposed approach with deep-learned features [66−72, 7] to improve the quality of the segmentation and make it more semantic.

**Author Contributions:** Conceptualization, K.E.K. and A.O.; formal analysis, Ay.B.; funding acquisition, A.B.; investigation, N.A. and S.J.; methodology, A.O. and K.E.K.; project administration, Ay.B. and A.O.; supervision, K.E.K. and A.O.; validation, A.B., M.H. and A.O.; writing—original draft preparation, N.A. and M.H.; writing—review and editing, A.B., S.J. and A.O. All authors have read and agreed to the published version of the manuscript.

**Funding:** This research received no external funding.

**Conflicts of Interest:** The authors declare no conflict of interest.

## References

1. Park, J. H.; de Lomana, A. L. G.; Marzese, D. M.; Juarez, T.; Feroze, A.; Hothi, P.; Cobbs, C.; Patel, A. P.; Kesari, S.; Huang, S.; Baliga, N. S. A Systems Approach to Brain Tumor Treatment. *Cancers* **2021**, *13*, 3152. [CrossRef]
2. Sandler, C. X.; Matsuyama, M.; Jones, T. L.; Bashford, J.; Langbeker, D.; Hayes, S. C. Physical activity and exercise in adults diagnosed with primary brain cancer: a systematic review. *J. Neurooncol.* **2021**, *153*, 1−14. [CrossRef]
3. Kanmounye, U. S.; Karekezi, C.; Nyalundja, A. S.; Awad, A. K.; Laeke, T.; Balogun, J. A. Adult brain tumors in Sub-Saharan Africa: A scoping review. *J. Phys.: Conf. Ser.* **2021**, *2115*, 1−20. [CrossRef]
4. Ali, S.; Li, J.; Pei, Y.; Khurram, R.; Rehman, K. U.; Mahmood, T. A Comprehensive Survey on Brain Tumor Diagnosis Using Deep Learning and Emerging Hybrid Techniques with Multi-modal MR Image. *Arch. Computat. Methods Eng.* **2022**. [CrossRef]
5. Bai, X.; Zhang, Y.; Liu, H.; Wang, Y. Intuitionistic Center-Free FCM Clustering for MR Brain Image Segmentation. *IEEE J. Biomed. Health Inform.* **2019**, *23*, 2039−2051. [CrossRef]
6. Li, S.; Liu, J.; Song, Z. Brain tumor segmentation based on region of interest-aided localization and segmentation U-Net. *Int. J. Mach. Learn. & Cyber.* **2022**. [CrossRef]
7. Di Ianni, T.; Airan, R. D. Deep-fUS: A Deep Learning Platform for Functional Ultrasound Imaging of the Brain Using Sparse Data. *IEEE Trans. Med. Imaging* **2022**, *41*, 1813−1825. [CrossRef]
8. Sastry, R.; Bi, W. L.; Pieper, S.; Frisken, S.; Kapur, T.; Wells, W.; Golby, A. J. Applications of Ultrasound in the Resection of Brain Tumors. *J. Neuroimaging* **2017**, *27*, 5−15. [CrossRef]
9. Guetbi, C.; Kouamé, D.; Ouahabi, A.; Remenieras, J.P. New emboli detection methods [Doppler ultrasound]. In Proceedings of the 1997 IEEE Ultrasonics Symposium Proceedings, An International Symposium (Cat. No.97CH36118), Toronto, On, Canada, 5−8 October 1997; pp. 1119−1122. [CrossRef]
10. Girault, J. M.; Kouamé, D.; Ouahabi, A.; Patat, F. Estimation of the blood Doppler frequency shift by a time-varying parametric approach. *Ultrasonics* **2000**, *38*, 682−687. [CrossRef]
11. Girault, J. M.; Ossant, F.; Ouahabi, A.; Kouame, D.; Patat, F. Time-varying autoregressive spectral estimation for ultrasound attenuation in tissue characterization. *IEEE Trans. Ultrason Ferroelectr. Freq. Control* **1998**, *45*, 650−659. [CrossRef]
12. Girault, M.; Kouame, D.; Ouahabi, A.; Patat, F. Micro-emboli detection: an ultrasound Doppler signal processing viewpoint. *IEEE Trans. Biomed. Eng.* **2000**, *47*, 1431−1439. [CrossRef]
13. Mesfin, F. B.; Al-Dhahir, M. A.; Gliomas. *Treasure Island* **2022**. Available from: https://www.ncbi.nlm.nih.gov/books/NBK441874/
14. https://www.arcagy.org/infocancer/localisations/autres-types-de-cancers/tumeurs-cerebrales/formes-de-la-maladie/les-gliomes.html/. Accessed on July 6, 2022.
15. Chen, Y.-W.; Hanak, B. W.; Yang, T.-C.; Wilson, T. A.; Hsia, J. M.; Walsh, H. E.; Shih, H.-C.; Nagatomo, K. J. Computer-assisted surgery in medical and dental applications. *Expert Rev. Med. Devices* **2021**, *18*, 669−696. [CrossRef]

16. Yaseen, S. F.; Al-Araji, A. S.; Humaidi, A. J. Brain tumor segmentation and classification: A one-decade review. *Int. J. Nonlinear Anal. Appl. In Pres* **2022**, 1−13. [CrossRef]
17. Ouahabi, A. Image Denoising using Wavelets: Application in Medical Imaging. In *Advances in Heuristic Signal Processing and Applications*; Chatterjee, A., Nobahari, H., Siarry, P., Eds.; Springer: Basel, Switzerland, 2013; pp. 287–313.
18. Razzak, I.; Imran, M.; Xu, G. Efficient Brain Tumor Segmentation with Multiscale Two-Pathway Group Conventional Neural Networks. *IEEE J. Biomed. Health Inform.* **2019**, *23*, 1911−1919. [CrossRef]
19. Zehani, S.; Ouahabi, A.; Oussalah, M.; Mimi, M.; Taleb-Ahmed, A. Bone microarchitecture characterization based on fractal analysis in spatial frequency domain imaging. *Int. J. Imaging Syst. Technol.* **2021**, *31*, 141−159. [CrossRef]
20. Vishnuvarthanan, G.; Rajasekaran, M.P.; Subbaraj, P.; Vishnuvarthanan, A. An unsupervised learning method with a clustering approach for tumor identification and tissue segmentation in magnetic resonance brain images. *Appl. Soft Comput.* **2016**, *38*, 190−212. [CrossRef]
21. Sujan, M.; Alam, N.; Abdullah, S.; Jahirul, M. A segmentation based automated system for brain tumor detection. *Int. J. Comput. Appl.* **2016**, 153, 41−49. [CrossRef]
22. Ilhan, U.; Ilhan, A. Brain tumor segmentation based on a new threshold approach. *Procedia Computer Science* **2017**, *120*, 580−587. [CrossRef]
23. Djeddi, M.; Ouahabi, A.; Batatia, H.; Basarab, A.; Kouame, D. Discrete wavelet transform for multifractal texture classification. Application to ultrasound imaging. In Proceedings of the 2010 IEEE International Conference on Image Processing (ICIP), Hong Kong, China, 26−29 September 2010; pp. 637−640. [CrossRef]
24. Deng, W.; Xiao, W.; Deng, H.; Liu, J. MRI brain tumor segmentation with region growing method based on the gradients and variances along and inside of the boundary curve. In Proceedings of the 2010 3rd International Conference on Biomedical Engineering and Informatics, Yantai, China, 16−18 October 2010; pp. 393−396. [CrossRef]
25. Węgliński, T.; Fabijańska, A. Brain tumor segmentation from MRI data sets using region growing approach. In Proceedings of the 2011 Perspective Technologies and Methods in MEMS Design, Polyana, Ukraine, 11−14 May 2011; pp. 185−188.
26. Hamiane, M.; Saeed, F. SVM Classification of MRI Brain Images for Computer-Assisted Diagnosis. *Int. J. Electr. Comput. Eng.* **2017**, *7*, 2555−2564. [CrossRef]
27. Zhang, N.; Ruan, S.; Lebonvallet, S.; Liao; Q.; Zhu; Y. Kernel feature selection to fuse multi-spectral MRI images for brain tumor segmentation. *Comput. Vis. Image Underst.* **2011**, *115*, 256–69. [CrossRef]
28. Koley, S.; Sadhu, A.K.; Mitra, P.; Chakraborty, B.; Chakraborty, C. Delineation and diagnosis of brain tumors from post contrast T1-weighted MR images using rough granular computing and random forest. *Appl. Soft Comput.* **2016**, *41*, 453−65. [CrossRef]
29. Havaei, M.; Davy, A.; Warde-Farley, D.; Biard, A.; Courville, A.; Bengio, Y.; Pal, C.; Jodoin, P.M.; Larochelle, H. Brain tumor segmentation with Deep Neural Networks. *Med. Image Anal.* **2017**, *35*, 18−31. [CrossRef]
30. Ma, C.; Luo, G.; Wang, K. Concatenated and connected random forests with multiscale patch driven active contour model for automated brain tumor segmentation of MR images. *IEEE Trans. Med. Imaging* **2018**, *37*, 1943−1954. [CrossRef]
31. Ben George, E.; Rosline, G.; Rajesh, D. Brain tumor segmentation using Cuckoo search optimization for magnetic resonance images. In Proceedings of the 2015 IEEE 8th GCC Conference & Exhibition, Muscat, Oman, 1−4 February 2015; pp. 1−6. [CrossRef]
32. Karnan, M.; Logheshwari, T. Improved implementation of brain MRI image segmentation using ant colony system. In Proceedings of the 2010 IEEE International Conference on Computational Intelligence and Computing Research (ICCIC), Coimbatore, India, 28−29 December 2010; pp. 1−4. [CrossRef]
33. Larson, M. G. Analysis of variance. *Circulation* **2008**, *117*, 115−121. [CrossRef]
34. Sun, H.; Wang, W. A new algorithm for unsupervised image segmentation based on D-MRF model and ANOVA. In Proceedings of the 2009 IEEE International Conference on Network Infrastructure and Digital Content (IC-NIDC), Beijing, China, 6−8 November 2009; pp. 754−758. [CrossRef]
35. Bonabeau, E.; Dorigo, M.; Theraulaz, G. Swarm intelligence: from natural to artificial systems. *Connection Science* **2002**, *14*, 163−164. [CrossRef]
36. Eberhart, R. C.; Kennedy, J. Particle Swarm Optimization. In Proceedings of 1995 IEEE International Conference on Neural Networks (ICNN), Perth, WA, Australia, 27 November−1 December 1995; pp. 1942−1948. [CrossRef]
37. Kirkpatrick, S.; Gelatt, C. D.; Vecchi, M. P. Optimization by simulated annealing. *Science* **1983**, *220*, 671−680. [CrossRef]
38. Mirjalili, S.; Mirjalili, S. M.; Lewis, A. Grey wolf optimizer. *Adv. Eng. Softw.* **2014**, *69*, 46−61. [CrossRef]
39. Salleh, M. N. M.; Hussain, K.; Cheng, S.; Shi, Y.; Muhammad, A.; Ullah, G.; Naseem, R. Exploration and Exploitation Measurement in Swarm-Based Metaheuristic Algorithms: An Empirical Analysis. In *Advances in Intelligent Systems and Computing;* Ghazali, R.; Deris, M. M.; Nawi, N. M.; Abawajy J. H.; Eds.; Springer International Publishing, 2018; pp. 24-32.
40. Boussaid, I.; Lepagnot, J.; Siarry, P. A survey on optimization metaheuristics. *Inf. Sci.* **2013**, *237*, 82−117. [CrossRef]
41. Thangaraj, R.; Pant, M.; Abraham, A.; Bouvry, P. Particle swarm optimization: hybridization perspectives and experimental illustrations. *Appl. Math. Comput.* **2011**, *217*, 5208−5226. [CrossRef]

42. Abdulraqeb, A. R. A.; Al-Haidri, W. A.; Sushkova, L. T. A novel segmentation algorithm for MRI brain tumor images. In Proceedings of the 2018 Ural Symposium on Biomedical Engineering, Radioelectronics and Information Technology (USBEREIT), Yekaterinburg, Russia, 7−8 May 2018; pp. 1−4. [CrossRef]
43. Dhanve, V.; Kumar, M. Detection of brain tumor using k-means segmentation based on object labeling algorithm. In Proceedings of the 2017 IEEE International Conference on Power, Control, Signals and Instrumentation Engineering (ICPCSI), Chennai, India, 21−22 September 2017; pp. 944−951. [CrossRef]
44. Ferroukhi, M.; Ouahabi, A.; Attari, M.; Habchi, Y.; Taleb-Ahmed, A. Medical video coding based on 2nd-generation wavelets: Performance evaluation. *Electronics* **2019**, *8*, 88. [CrossRef]
45. Mahdaoui, A. E.; Ouahabi, A.; Moulay, M. S. Image Denoising Using a Compressive Sensing Approach Based on Regularization Constraints. *Sensors* **2022**, *22*, 2199. [CrossRef]
46. Haneche, H.; Ouahabi, A.; Boudraa, B. New mobile communication system design for Rayleigh environments based on compressed sensing-source coding. *IET Commun.* **2019**, *13*, 2375−2385. [CrossRef]
47. Haneche, H.; Boudraa, B.; Ouahabi, A. A new way to enhance speech signal based on compressed sensing, *Measurement* **2020**, 151, 107−117. [CrossRef]
48. Haneche, H.; Ouahabi, A.; Boudraa, B. Compressed sensing-speech coding scheme for mobile communications. *Circuits, Syst. Signal Process.* **2021**, *40*, 5106−5126. [CrossRef]
49. Kim, J.; Wang, Q.; Zhang, S.; Yoon, S. Compressed Sensing-Based Super-Resolution Ultrasound Imaging for Faster Acquisition and High Quality Images. *IEEE Trans. Biomed. Eng.* **2021**, *68*, 3317−3326. [CrossRef]
50. Ouahabi, A. A review of wavelet denoising in medical imaging. In Proceedings of the 2013 8th International Workshop on Systems, Signal Processing and their Applications (WoSSPA), Algiers, Algeria, 12−15 May 2013; pp.19−26. [CrossRef]
51. Sidahmed, S.; Messali, Z.; Ouahabi, A.; Trépout, S.; Messaoudi, C.; Marco, S. Nonparametric Denoising Methods Based on Contourlet Transform with Sharp Frequency Localization: Application to Low Exposure Time Electron Microscopy Images. *Entropy* **2015**, *17*, 3461−3478. [CrossRef]
52. Ouahabi, A. *Signal and Image Multiresolution Analysis*, 1st ed.; ISTE-Wiley: London, UK, 2012.
53. Demirhan, A.; Törü, M.; Güler, I. Segmentation of tumor and edema along with healthy tissues of brain using wavelets and neural networks. *IEEE J. Biomed. Health Inform.* **2015**, *19*, 1451−1458. [CrossRef]
54. Smith, S. M. Fast robust automated brain extraction. *Human brain mapping* **2002**, *17*, 143−155. [CrossRef]
55. Iglesias, J. E.; Liu, C. Y.; Thompson, P. M.; Tu, Z. Robust brain extraction across datasets and comparison with publicly available methods. *IEEE Trans. Med. Imaging* **2011**, *30*, 1617−1634. [CrossRef]
56. Ashburner, J.; Friston, K. J. Unified segmentation. *Neuroimage* **2005**, *26*, 839−851. [CrossRef]
57. Vishnuvarthanan, A.; Rajasekaran, M. P.; Vishnuvarthanan, G.; Zhang, Y.; Thiyagarajan, A. An automated hybrid approach using clustering and nature inspired optimization technique for improved tumor and tissue segmentation in magnetic resonance brain images. *Appl. Soft Comput.* **2017**, *57*, 399−426. [CrossRef]
58. Akkus, A.; Galimzianova, A.; Hoogi, A.; Rubin, D. L.; Erickson, B. J. Deep learning for brain MRI segmentation: state of the art and future directions. *J. Digit Imaging* **2017**, *30*, 449−459. [CrossRef]
59. Cai, J.; Pan, W. D. On fast and accurate block-based motion estimation algorithms using particle swarm optimization. *Inf. Sci.* **2012**, *197*, 53−64. [CrossRef]
60. Goshtasby, A. Image registration: Principles, tools and methods. Science, Business Media. Springer, 2012.
61. Center of Imaging of Kouba, Algeria Database: https://figshare.com/articles/brain_tumor_dataset/1512427, Accessed on March 24, 2022.
62. Souibgui, M. A.; Kessentini, Y. DE-GAN: A Conditional Generative Adversarial Network for Document Enhancement. *IEEE Trans. Pattern Anal. Mach. Intell.* **2022**, *44*, 1180−1191. [CrossRef]
63. Gui, J.; Sun, Z.; Wen, Y.; Tao, T.; Ye, J. A Review on Generative Adversarial Networks: Algorithms, Theory, and Applications. *IEEE Trans. Knowl. Data Eng.* **2021**. [CrossRef]
64. Khaldi, Y.; Benzaoui, A. A new framework for grayscale ear images recognition using generative adversarial networks under unconstrained conditions. *Evol. Syst.* **2021**, *12*, 923−934. [CrossRef]
65. Creswell, A.; Bharath, A. A. Inverting the Generator of a Generative Adversarial Network. *IEEE Trans. Neural Netw. Learn. Syst.* **2019**, *30*, 1967−1974. [CrossRef]
66. Adjabi, I.; Ouahabi, A.; Benzaoui, A.; Taleb-Ahmed, A. Past, present, and future of face recognition: A Review. *Electronics* **2020**, *9*, 1188. [CrossRef]
67. Adjabi, I.; Ouahabi, A.; Benzaoui, A.; Jacques, S. Multi-block color-binarized statistical images for single-sample face recognition. *Sensors* **2021**, *21*, 728. [CrossRef]
68. El Morabit, S.; Rivenq, A.; Zighem, M. E.; Hadid, A.; Ouahabi, A.; Taleb-Ahmed, A. Automatic Pain Estimation from Facial Expressions: A Comparative Analysis Using Off-the-Shelf CNN Architectures. *Electronics* **2021**, *10*, 1926. [CrossRef]
69. Khaldi, Y.; Benzaoui, A.; Ouahabi, A.; Jacques, S.; Taleb-Ahmed, A. Ear recognition based on deep unsupervised active learning. *IEEE Sens. J.* **2021**, *21*, 20704−20713. [CrossRef]
70. Arbaoui, A.; Ouahabi, A.; Jacques, S.; Hamiane, M. Concrete Cracks Detection and Monitoring Using Deep Learning-Based Multiresolution Analysis. *Electronics* **2021**, *10*, 1772. [CrossRef]

 doi:10.20944/preprints202207.0211.v1

71. Arbaoui, A.; Ouahabi, A.; Jacques, S.; Hamiane, M. Wavelet-based multiresolution analysis coupled with deep learning to efficiently monitor cracks in concrete. *Frat. ed Integrita Strutt.* **2021**, *58*, 33−47. [CrossRef]
72. Benlamoudi, A.; Bekhouche, S. E.; Korichi, M.; Bensid, K.; Ouahabi, A.; Hadid, A.; Taleb-Ahmed, A. Face Presentation Attack Detection Using Deep Background Subtraction. *Sensors* **2022**, 22, 3760. [CrossRef]